Structural-modulation-driven spin canting and reentrant glassy magnetic phase in ferromagnetic Lu_2MnNiO_6

Kaustuv Manna,[1,2] A. K. Bera,[3,4] Manish Jain,[1] Suja Elizabeth,[1] S. M. Yusuf,[3] and P. S. Anil Kumar[1]
[1]*Department of Physics, Indian Institute of Science, Bangalore 560012, India*
[2]*Leibniz-Institute for Solid State and Materials Research, (IFW)-Dresden, D-01171 Dresden, Germany*
[3]*Solid State Physics Division, Bhabha Atomic Research Centre, Mumbai 400085, India*
[4]*Helmholtz-Zentrum Berlin für Materialien und Energie, D-14109 Berlin, Germany*
(Received 26 January 2015; revised manuscript received 10 May 2015; published 15 June 2015)

Unusual behavior of reentrant spin-glass (RSG) compound Lu_2MnNiO_6 has been investigated by magnetometry and neutron diffraction. The system possesses a ferromagnetic (FM) ordering below 40 K and undergoes a RSG transition at 20 K. Additionally, Lu_2MnNiO_6 retains memory effect above the glassy transition till spins sustain ordering. A novel critical behavior with unusual critical exponents ($\beta =\sim 0.241$ and $\gamma \sim 1.142$) is observed that indicates a canting in the spin structure below the ferromagnetic transition (T_C). A comprehensive analysis of temperature-dependent neutron diffraction data and first-principles calculations divulge that a structural distortion induced by an octahedral tilting results in a canted spin structure below T_C.

DOI: 10.1103/PhysRevB.91.224420 PACS number(s): 64.60.F−, 75.50.Dd, 75.40.−s, 75.47.Lx

In the past few decades, spin frustration in magnetic systems has gotten immense interest for fundamental understanding as well as ultimately in practical applications [1–11]. Reentrant spin-glass (RSG) systems are of particular interest in this regard where competing ferromagnetic (FM) and antiferromagnetic (AFM) interactions lead to unusual behaviors. A RSG possesses a long-range FM or AFM ordering at high temperature and upon cooling undergoes a glassy transition at a lower temperature [12–14]. It is understood that at the glassy transition, the FM and AFM strengths come to an equivalent order and spins become frustrated. But its detail mechanism is an open question and is under investigation. Numerous experimental [15] as well as theoretical [16] investigations were undertaken to establish the origin of low-temperature glassiness. It was predicted that the competing interaction of short-range FM and long-range RKKY type leads to a canted spin structure, resulting in RSG behavior of Au-Fe alloys [17–19]. In itinerant FM $SrRuO_3$, structural modulation driven by the octahedral tilting provokes the low-temperature glassiness [20]. In rare-earth (R) double perovskites, lattice distortion adds another level of complexity. With the decrease in R-site ionic radius, internal pressure increases and octahedral tilting results in concurrent reduction in exchange magnetic interaction [21,22]. The spin-orbit interaction (SOI) also has an important role in this regard [23].

We report the results of a new RSG perovskite compound Lu_2MnNiO_6 (LMNO), where the giant octahedral distortion induced by the smallest of rare-earth ions, Lu, helps us to reveal the hidden interactions in perovskite RSG compounds. This material shows a FM ordering below ∼40 K and undergoes a RSG transition at ∼20 K. This article describes a comprehensive investigation of magnetometry, memory, critical behavior, temperature-dependent neutron diffraction, and first-principles theoretical calculation concerning the anomalous RSG behavior in Lu_2MnNiO_6.

Polycrystalline LMNO samples have been prepared by standard nitrate decomposition method using Lu_2O_3, MnO_2, and NiO precursors. After dissolving all the constituents in concentrated HNO_3, the mixture was calcined at 400 °C. The solid residue was heated to 1000 °C with intermediate grinding and annealing. The phase formation was monitored at different stages of sample preparation by powder x-ray diffraction (XRD) using a Bruker D8 Advance diffractometer with Cu Kα radiation. Neutron diffraction (ND) experiments were performed using the neutron powder diffractometer ($\lambda = 1.2443$Å) with five linear position-sensitive detectors at Dhruva reactor, Bhabha Atomic Research Centre, India. dc magnetization measurements were carried out using a quantum design 14 T physical property measurement system (PPMS) and ac susceptibility in a commercial CryoBIND system down to 4.2 K in the frequency range, 9 Hz to 10 kHz.

The crystallographic details were analyzed using the Rietveld refinement of the ND patterns at various temperatures using the FULLPROF program suite [24,25]. The compound crystallizes in the monoclinic $P2_1/n$ space group. At 300 K, the lattice parameters a, b, and c were derived as: 5.1451(6) Å, 5.5149(6) Å, and 7.4044(8) Å, respectively, with angle ß = 90.32(1)°. The magnetic ions (Ni and Mn) are situated in the Ni/MnO_6 octahedral environment. The NiO_6 and MnO_6 octahedra arrange alternatively along the three crystallographic directions. Due to the small size of Lu^{3+} cation, both Ni and Mn octahedra are found to be titled in all three directions. The detailed analysis is presented in Appendix A. Pictorial representations of the crystal structure are presented in Fig. 1.

Temperature-dependent, field-cooled (FC), and zero-field -cooled (ZFC) magnetization (M_{FC} and M_{ZFC}) at 50 Oe applied dc magnetic field is illustrated in Fig. 2(a). Brillouin-like behavior in $M_{FC}(T)$, classifies LMNO as a ferromagnet till the lowest temperature. A linear Curie-Weiss fit in the paramagnetic region of the inverse dc susceptibility ($\chi_{dc}{}^{-1}$) [top inset of Fig. 2(a)] confirms the absence of any high-temperature ordered magnetic phase. The M–H loop [bottom, inset of Fig. 2(a)] recorded at 2 K and field up to 14 T signifies the soft FM behavior of the compound [coercive field, $H_C = 501$ Oe] with saturation magnetization, $M_{SM} = 2.2\ \mu_B$/FU. Figure 2(b) displays the temperature dependence of zero-field-cooled

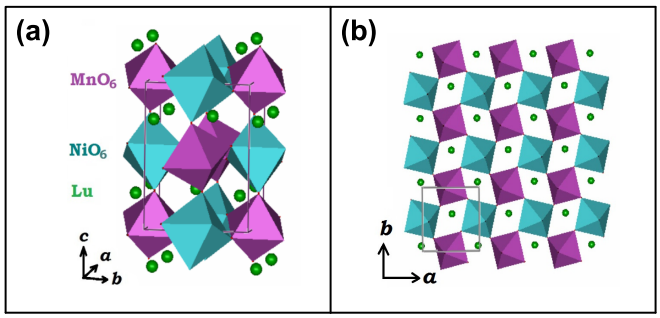

FIG. 1. (Color online) (a) Octahedral tilting in Lu_2MnNiO_6 crystal structure generated from the refinement of room-temperature neutron diffraction pattern. (b) The checkerboardlike arrangement of MnO_6 and NiO_6 octahedra within the *ab* plane.

in-phase [$\chi'(T)$; inset] and out-of-phase [$\chi''(T)$] components of ac susceptibility χ_{ac} with probing ac field of $H_{ac} = 0.17$ Oe. T_C is found to be at 40.01 K, and upon further cooling, a hump appears around $T_f = 25$ K. The effect is observed to be more prompt in $\chi''(T)$. It is evident that T_f shifts to a higher value with increasing frequency of H_{ac}. The spin-flip time is derived to be $4.20(36) \times 10^{-4}$s (for detailed analysis see Appendix B). Also, on imprinting a dc biasing field (H_{dc}), amplitude of T_C falls sharply with increasing H_{dc} [Fig. 2(c)], as expected for FMs. But a minor variation happens at T_f. T_f shifts to a lower value with the increase in H_{dc} [Fig. 2(c) inset]. It is likely that the strong H_{dc} hinders the random freezing process and thereby shifts T_f to a lower value. All experimental observations clearly evidence LMNO as a RSG compound. To understand more about this a competing FM and AFM interactions memory experiment was performed in the same protocol as explained earlier [4,5,12]. A dip in the memory experiment [$\chi''_{mem}(T)$] at the halting temperature [T_{halt}] evidence the memory effect in LMNO. The difference of $\chi''_{mem}(T)$ and reference measurement, $\chi''_{ref}(T)$ is presented in the inset of Fig. 2(d). It is striking that LMNO shows an unusual behavior where memory exists above T_f also. This suggests that an AFM interaction induces in the system along with the dominant FM ordering below T_C. Due to this vying effect of FM and AFM interaction, the system possesses memory all over below T_C.

We performed the critical behavior study around the corresponding T_C [266] to understand the nature of the magnetic interaction in LMNO. For this, we recorded 20 $M(H)$ isotherms in the temperature window 28–52 K with field up to 14 T. It is significant to note that the scaled plot according to the Arrott method [27] (M^2 vs H/M) does not show progressive parallel lines, which suggests that the magnetic interaction in LMNO is not the mean-field type. So, a modified Arrott plot was used to determine the critical exponents, which follow the Arrott-Noaks equation of state as: $(H/M)^{1/\gamma} = A\varepsilon + B(M)^{1/\beta}$, where A and B are constants [26,27]. The spontaneous magnetization (M_S) below T_C and initial susceptibility (χ_0) above T_C are first calculated from

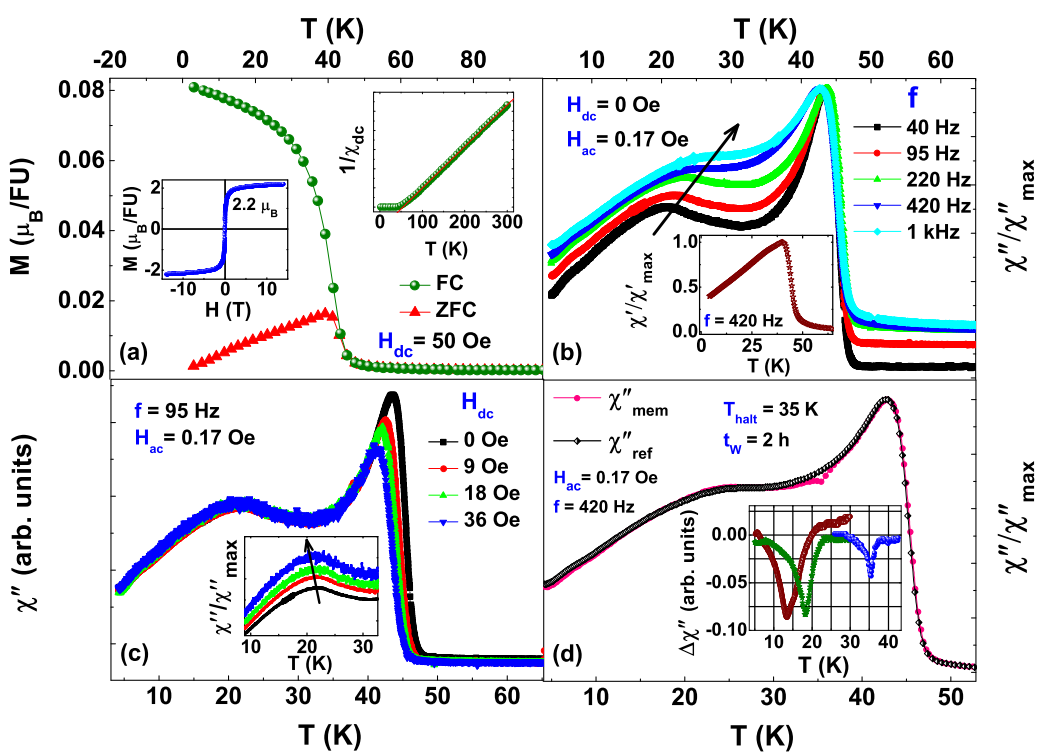

FIG. 2. (Color online) (a) Temperature-dependent FC and ZFC dc magnetization at 50 Oe applied field. Upper inset illustrates the corresponding inverse dc susceptibility ($\chi_{dc}{}^{-1}$) with straight line fit. The lower inset displays the hysteresis loop at 2 K. (b) $\chi''(T)$ at various frequencies of H_{ac}. Inset presents $\chi'(T)$ at H_{ac}= 0.17 Oe and frequency, 420 Hz. (c) dc biasing effect of $\chi''(T)$. The inset shows the corresponding zoomed-in view around the T_f in normalized scale. (d) Result of memory experiment with halting temperature: $T_{halt} = 35$ K and waiting time: $t_w = 2$ h. The inset illustrates the difference ($\Delta\chi'' = \chi''_{mem} - \chi''_{ref}$) at 13, 18, and 35 K.

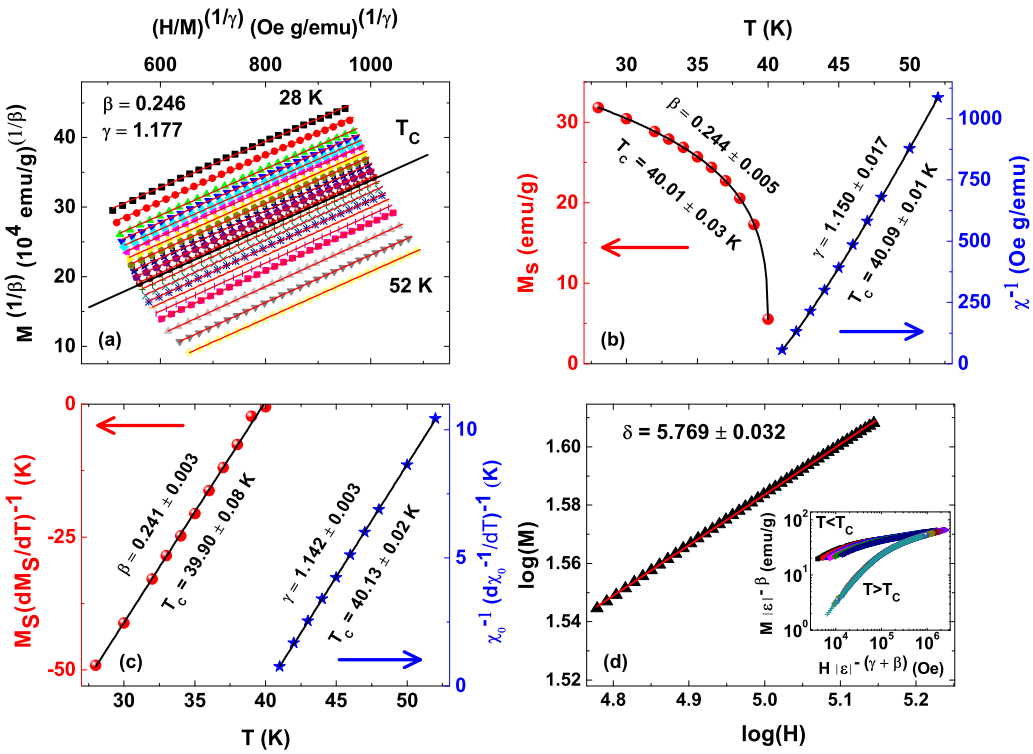

FIG. 3. (Color online) (a) Magnified view of the modified Arrott plot isotherms [$M^{1/\beta}$ vs $(H/M)^{1/\gamma}$] for Lu_2MnNiO_6 in 5–14 T range with $T = T_C$ isotherm passing through the origin. (b) Temperature dependence of the spontaneous magnetization [$M_S(T)$] and inverse initial susceptibility [$\chi_0{}^{-1}(T)$] [obtained from Arrott plot (a)] with power-law fittings. (c) The corresponding Kouvel-Fisher plot for Lu_2MnNiO_6 critical behavior. (d) Critical $M(H)$ isotherm close to the T_C in log-log scale with the straight line as linear fit. Inset illustrates a scaling plot of the M(H) isotherms below and above T_C in log-log scale with β and γ obtained from (c).

the Arrott plot through simple extrapolation of the high field data. β and γ are estimated from the power-law fit of $M_S(T)$ and $\chi_0{}^{-1}(T)$ respectively. Subsequently, a modified Arrott plot was constructed. A self-consistent method was employed to obtain a set of optimum values of β and γ so that the $M^{1/\beta}$ vs $(H/M)^{1/\gamma}$ plots [Fig. 3(a)] form parallel straight lines with the isotherm $T = T_C$ passing through origin. The critical exponent values match very well with those calculated from the power-law fitting. The T_{C+} and T_{C-} are identical as illustrated in Fig. 3(b). Only the high field data (5–14 T) was considered for this analysis where all FM domains are aligned in the applied field direction. For a precise determination of the exponents and verification of the T_C, the Kouvel-Fisher (KF) method [28] was also utilized. β and γ calculated from the slope of the temperature dependence of $M_S(dM_S/dT)^{-1}$ and $\chi_0{}^{-1}(d\chi_0{}^{-1}/dT)^{-1}$ are: 0.241(3) and 1.142(3), respectively [Fig. 3(c)]. The critical exponent δ is estimated from the $M(H)$ isotherm at $T = T_C$, which follows the equation of state as $M(H,T_C) = C(H)^{1/\delta}$, C is critical amplitude. The linear fit to the plot in log-log scale is shown in Fig. 3(d) and yields $\delta = 5.77(3)$. This conforms to the δ calculated using the exponents from Fig. 3(c) and the scaling law, $\delta = (1 + \gamma/\beta) = 5.74$. According to the scaling hypothesis [26], the scaling plot in the inset of Fig. 3(d) confirms that the calculated critical exponents are intrinsic to the system and unambiguous.

To resolve the class of magnetic interaction in LMNO, different exponents obtained in the present work along with results of referred theoretical models [26] are compared in Table I. It is evident that the critical exponents for LMNO don't match with any of the conventional theories such as the mean-field, 3D Heisenberg, or 3D Ising. Rather, they are in good agreement with those calculated for the magnets possessing the 3D version of $(Z_2 \times S_1)$ symmetry [29]. Symmetry of this kind represents the canted FM structure similar to the first molecular ferromagnet $Fe[S_2CN(C_2H_5)_2]_2Cl$ [30–32]. This strongly suggests that the spin arrangement in LMNO is canted FM.

The microscopic spin arrangement is determined from the Rietveld refinement of the neutron thermodiffractograms. Figure 4(a) illustrates the temperature-dependent ND patterns in the range 6–50 K. The magnetic contribution is marked by an increase in the intensity of fundamental Bragg peaks at ~19° and 27.3° below 30 K. The magnetic peak at 19°

TABLE I. Comparison of critical exponents calculated for Lu_2MnNiO_6 with different theoretical models.

Material	β	γ	δ
Lu_2MnNiO_6	0.241(3)	1.142(3)	5.77(3)
Mean-field theory	0.5	1.0	3.0
3D Heisenberg model	0.365	1.386	4.8
3D Ising model	0.325	1.241	4.82
3D $(Z_2 \times S_1)$ model	0.25(1)	1.13(5)	5.47(27)

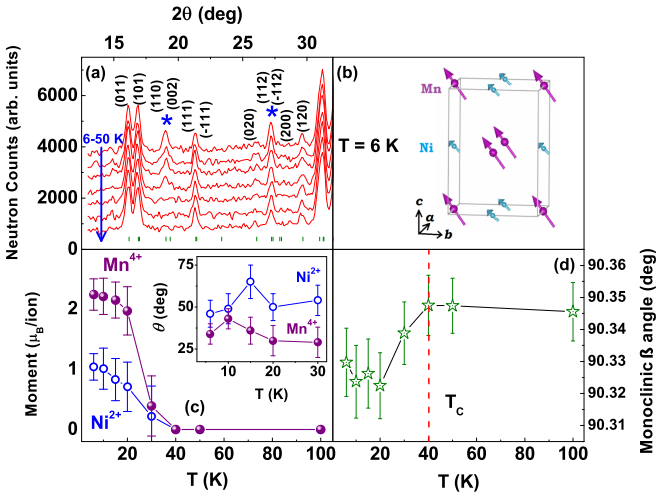

FIG. 4. (Color online) (a) Neutron diffraction (ND) patterns at 6, 10, 15, 20, 30, 40, and 50 K with the highlighted peaks having magnetic contribution. (b) Canted ferromagnetic spin arrangement of Mn^{4+} and Ni^{2+} generated from the Rietveld refinement of the 6 K ND pattern. (c) Temperature dependence of the refined ordered magnetic moment extracted from ND. The corresponding inset presents the temperature dependent angle (θ) for the magnetic ions. (d) Temperature variation of the monoclinic angle (ß), extracted from the ND patterns.

is indexed with (110) and (002) whereas, the 27.3° peak is associated with (112) and (–112) of monoclinic $P2_1/n$ unit cell. There is no satellite magnetic Bragg peak. This implies the presence of a FM-type ordering. The bond valence sum (BVS) calculation yields 2+ and 4+ as the oxidation states of Ni and Mn, respectively. The magnetic refinement is carried out considering the magnetic form factors of Ni^{2+} and Mn^{4+} ions. A model with a canted FM structure best fits the measured magnetic pattern. A schematic of this spin arrangement at 6 K is pictured in Fig. 4(b). All spins within a given sublattice [Ni ($2a$) and Mn ($2b$)] order ferromagnetically, but form an angle with spins in the other sublattice. The spins for both the sublattices lie in the bc plane and tilt with respect to the crystallographic c axis ($\theta \sim 30 - 60°$). The temperature-dependent θ values for both the sublattices are shown in the inset of Fig. 4(c). The difference in the θ values represents the spin canting, which remains finite down to 6 K [inset of Fig. 4(c)]. This reveals that the canted spin structure is stable down to the lowest measured temperature. The temperature dependences of the refined ordered magnetic moments of $Mn^{4+}(3d^3)$ and $Ni^{2+}(3d^8)$ are plotted in Fig. 4(c). As the sample is cooled, the moment increases following a Brillouin-like behavior and saturates at low temperature. It is found that the ordered moment values for both Mn and Ni ions at 6 K[2.24(26) μ_B/Mn and 1.04(22) μ_B/Ni, respectively] are quite small as compared to the theoretically predicted spin-only ordered moment values (3 μ_B/Mn and 2 μ_B/Ni, respectively). This indicates the presence of competing FM and AFM interactions in the system. Such reduced moments are comparable to those of Co and Os ions in Sr_2CoOsO_6 as observed by Yan *et al.* [33]. Here, the average effective moment (seen by neutron diffraction) undergoes magnetic long-range order at 108 K with reduced ordered moments. This was referred due to the dynamical fluctuations of Co and Os spins. With cooling, Co moments become frozen at $\sim$ 67 K and result in a canted AFM order. With further decreasing temperature, the Os moments are frozen into a randomly canted state resulting in a glassy transition (RSG state). Since neutron diffraction measures the average effective moment, no anomaly was found around 6 K. However, the glassy transition around 6 K was clearly seen in the ac susceptibility. At base temperature (2 K), the ordered moment values were reported to be 2.7 μ_B and 0.7 μ_B for Co ($S = 3/2$) and Os ($S = 1$), respectively. In summary, the glassy transition in Sr_2CoOsO_6 was reported to be due to the randomly frozen Os moments alone. In this regard, the detailed spin structure of LMNO requires further investigation. The temperature dependence of the monoclinic angle ß [Fig. 4(d)] shows that the monoclinic distortion slightly decreases below T_C indicating that a reduced distortion helps to establish a long-range ferromagnetic ordering. Nevertheless, the residual monoclinic distortion seems to be responsible for the observed canting in the ferromagnetic structure below T_C. With further decrease of temperature the monoclinic angle ß attains a constant value around T_f. Interestingly, the glassy transition and the freezing of the monoclinic distortion in LMNO occurs around the same temperature. Because of the polycrystalline averaging and weak ferromagnetic signal, no observable changes in the FM ordered state are found below T_f. A single-crystal-based reexamination might be useful in this regard.

The electronic structure of LMNO was better understood by performing first-principles calculations using the pseudopotential density functional method as implemented in QUANTUM ESPRESSO [34]. We employed the wavefunction cutoff at 150 Ry and ($5 \times 5 \times 5$) mesh of k points to sample the Brillouin zone. We used fully relativistic norm-conserving pseudopotentials for all the calculations. The spin-polarized PBE [35] exchange correlation function was used in the density of states (DOS) calculation. In order to search for the lowest-energy spin configurations, we performed noncollinear total energy calculations including spin orbit interaction. All calculations were carried out considering the experimental lattice constants of the monoclinic unit cell (derived from the neutron diffraction study) containing 20 atoms.

Figure 5(a) shows the spin-resolved DOS of LMNO. The atom-resolved partial DOS are presented in Figs. 5(b)–5(e). Figure 5(b) reveals that at $\sim$2 eV below the Fermi level, the predominant contribution comes from O-p states. Lu-f states as shown in Fig. 5(e) occur at $\sim$4 eV below the Fermi level. The octahedra of oxygen atoms surrounding the Mn and Ni atoms causes the d manifold to split in t_{2g} and e_g levels. Figures 5(c) and 5(d) show the partial density of states contribution from Mn-d and Ni-d states respectively. In the spin-up channel, Ni-t_{2g} and Ni-e_g are occupied by states within -2 eV of the Fermi level. These states possess significant hybridization with the O-p states as well as Mn-d states. For the spin-down channel, however, the Ni-t_{2g} levels are occupied while the Ni-e_g levels lie above the Fermi level. This corresponds to the nominal oxidation state of Ni (2+). For the Mn-d levels, only the Mn-t_{2g} levels in the spin-up channel lie below the Fermi level, while Mn-e_g levels in the spin-up channel and Mn-t_{2g} and Mn-e_g levels in the spin-down channel lie above the Fermi

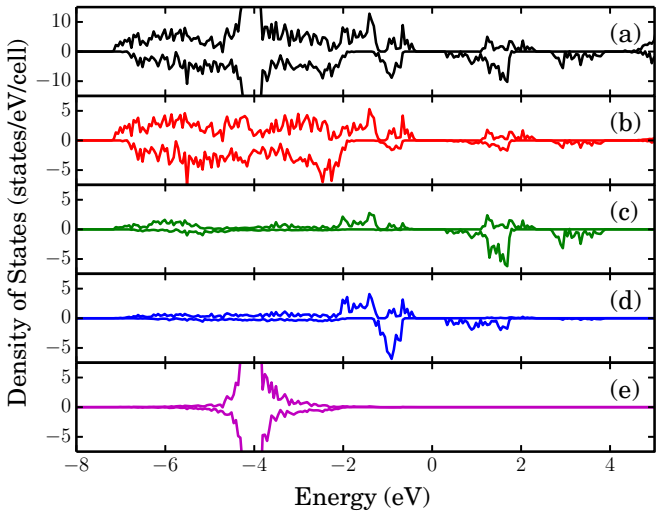

FIG. 5. (Color online) (a) Density of states of Lu_2MnNiO_6. Partial density of states from (b) O-p, (c) Mn-d, (d) Ni-d, and (e) Lu-f states.

level. This conforms to an oxidation state of Mn^{4+}, which is consistent with the neutron diffraction results. Our results for the partial and total DOS are similar to those of La_2NiMnO_6 [36]. The total magnetic moment within the spin-polarized calculations was $5\,\mu_B$/FU, in good conformance with the experimental dc magnetization value of $4.4\,\mu_B$/FU. The Mn moment was calculated as $2.95\,\mu_B$/FU within the radius of 1.32 Å while the moment at the Ni site was $1.50\,\mu_B$/FU within a radius of 1.52 Å. The remaining moment is at the O sites. Overall, this is in reasonable agreement with the experimental results of $2.24(26)\,\mu_B$/Mn and $1.04(22)\,\mu_B$/Ni at 6K (Fig. 4).

Furthermore, we found the FM state (without any canting) to be the lowest-energy spin configuration. However, the canted spin structure was only nominally higher by about 1 meV/FU. Such a small energy difference is within the error bar of our calculation. This is consistent with the T_C of 40 K. The small energy difference suggests that the canting of the spins could be largely driven by octahedral distortions.

In summary, the detailed magnetometry establishes Lu_2MnNiO_6 as a reentrant spin-glass compound. The anomolous memory effect reveals that an AFM interaction induces in LMNO along with the dominant FM ordering below T_C. This is further supported by the reduced ordered moment of Mn/Ni ions in neutron diffraction. The unusual critical exponents of $\beta \sim 0.241(3)$, $\gamma \sim 1.142(3)$, and $\delta = 5.77(3)$ hints at the presence of a canted spin structure. The temperature-dependent neutron diffraction reveals a decrease of monoclinic distortion below T_C and attains a nearly constant value around the glassy transition. Our first-principles calculations suggest that the spin-orbit interaction together with monoclinic distortion below T_C may be responsible for the observed spin canting. This leaves a future scope of an experimental realization of the theoretically predicted spin-orbit interaction through a single-crystal study of anisotropy or angle-resolved photoemission spectroscopy. We strongly believe that the AFM interaction is induced from this canted spin structure and competes with the FM interaction to generate spin frustration. This is likely to serve as a guiding tool to investigate the origin of glassiness in similar RSG compounds.

ACKNOWLEDGMENTS

The authors acknowledge Department of Science and Technology, Ministry of Science and Technology, Government of India for providing financial assistance to carry out this research work. One of us (K.M.) acknowledges the Council of Scientific and Industrial Research (CSIR), Government of India for providing research fellowship.

APPENDIX A: CRYSTAL STRUCTURE OF Lu_2MnNiO_6 AT 300 K

Detailed crystal structural information of Lu_2MnNiO_6 was obtained by Rietveld analysis of the neutron diffraction pattern measured at 300 K. The result is displayed in Fig. 6. The compound crystallizes in the monoclinic symmetry with space group: $P2_1/n$ ($\chi^2 = 2.45$; $R_{wp} = 3.89\%$; $R_p = 3.01\%$; $R_{\text{Bragg}} = 4.27\%$). The magnetic ions Ni and Mn populate at two crystallographically independent sites at $2a$ (0, 0, 0) and $2b$ (1/2, 1/2, 0) respectively. A small amount of intermixing of Ni/Mn occupancy (~6.6%) has been observed. The large difference in the neutron coherence scattering lengths of Ni and Mn (+10.30 and −3.73 fm, respectively) helps to determine the corresponding occupancy in different crystal sites. All three kinds of nonequivalent oxygen atoms (O1, O2, O3), as also the rare-earth Lu ions, are situated in general positions namely, $4e$ site (x, y, z). The magnetic ions (Ni and Mn) are situated in the Ni/MnO_6 octahedral environment. The basal planes of the Ni/MnO_6 octahedra are formed by two O2 and two O3 oxygen ions. However, they are connected by O1 ions along c axis. The various bond details and crystallographic information are listed in Table II. The

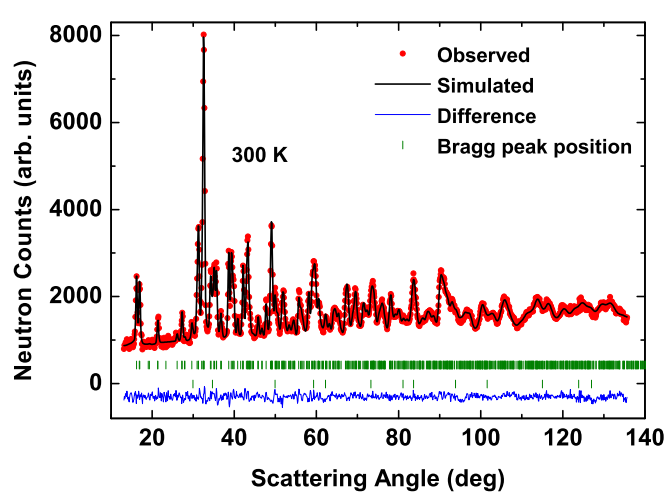

FIG. 6. (Color online) Neutron diffraction pattern of Lu_2MnNiO_6 at 300 K.

TABLE II. Results obtained from the Rietveld refinement of neutron diffraction pattern at 300 K.

Space Group		a (Å)	b (Å)	c (Å)	Angle ß (degree)		
$P2_1/n$		5.1451(6)	5.5149(6)	7.4044(8)	$\alpha = \gamma = 90$, ß $= 90.32(1)$		
Atoms	Wyckoff positions		x/a	y/b	z/c	B_{iso}	Occ.
Lu	4e		0.4775(7)	0.0752(6)	0.7501(6)	0.67(5)	1.0
Ni/Mn	2a		0	0	0	0.92(7)	0.467(2)/0.033(2)
Mn/Ni	2b		0.5	0.5	0	1.30(27)	0.467(2)/0.033(2)
O1	4e		0.6126(8)	0.4599(8)	0.7548(8)	0.65(6)	1.0
O2	4e		0.1762(9)	0.2971(9)	0.5578(8)	0.88(10)	1.0
O3	4e		0.6991(9)	0.1828(10)	0.4455(7)	0.60(8)	1.0
R_p:			3.01%	R_{Bragg}:	4.27%		
R_{wp}:			3.89%	χ^2:	2.52%		
R_{exp}:			2.45%				
Bond lengths							
		Ni-O	Mn-O		Lu-O		
O1		1.989(6) × 2	1.915(6) × 2	2.203(5)	2.233(6)		
O2		2.050(5) × 2	1.922(5) × 2	2.234(7)	2.440(6)	2.600(7)	
O3		2.067(5) × 2	1.892(5) × 2	2.227(7)	2.430(6)	2.590(7)	
Bond angles							
Ni-O1-Mn (along c)		Ni-O2-Mn (ab plane)	Ni-O3-Mn (ab plane)				
142.9(2)		143.4(2)	144.5(2)				

sample is a single phase, though a small trace of residual NiO is present.

APPENDIX B: ANALYSIS OF THE REENTRANT GLASSY PHASE IN Lu_2MnNiO_6

The temperature dependence of zero-field-cooled out-of-phase [$\chi''(T)$] component of ac susceptibility χ_{ac} data of Lu_2MnNiO_6 (LMNO) were recorded at frequencies $f =$ 40, 95, 220, 420 Hz, and 1 kHz with probing field of $H_{ac} = 0.17$ Oe. It is observed that $\chi''(T)$ abruptly decreases to a very low value above the ferromagnetic transition temperature (T_C), at 40 K and has no effect on the frequency variation of the applied ac magnetic field. However, the low-temperature hump (T_f) as described in the main text, shifts to a higher value as the frequency is increased. The maximum change observed in the magnitude of T_f is: $\Delta T_f = (T_f{}^{1\,\mathrm{kHz}} - T_f{}^{40\,\mathrm{Hz}}) = 6.9$ K. A quantitative analysis of the relative variation in T_f with frequency is expressed as, $s = \Delta T_f/[T_f \Delta \log_{10} f] = 0.204$, where, $\Delta T_f = (T_{f1} - T_{f2})$ and $\Delta \log_{10} f = [\log_{10} f_1 - \log_{10} f_2]$ with $f_1 = 1$ kHz and $f_2 =$ 40 Hz. This is above that of a typical spin-glass (SG) phase [$10^{-2} - 10^{-3}$], but lies within the range of the superparamagnetic state [$10^{-1} - 10^{-2}$] [4,5,37].

The frequency dependence of T_f can be described using the critical slowing down model [11,37–40] as: $T_f = \tau_0(T_f/T_g - 1)^{z\vartheta}$, where, $\tau_f \propto \mathrm{f}^{-1}$, τ_0 is the microscopic spin-flip time and $z\vartheta$ is the critical exponent. The above equation is validated in Fig. 7 where the $\log_{10} f$ is plotted as a function of $\log_{10}[(T_f/T_g) - 1]$. Under the best-fit condition τ_0, $z\vartheta$, and T_g attain the values of $4.20(36) \times 10^{-4}$s, 3.89(13), and 15.3(15) K, respectively. A large value of τ_0 indicates that the spin flipping is slower than in a conventional SG system ($\sim 10^{-13}$s). Such high τ_0 is reported for several SG [41,42] as well as RSG systems [43]. The origin of such behavior in LMNO is still uncertain. The observed value of $z\vartheta$ is similar to that found in $LaMn_{0.5}Fe_{0.5}O_3$ [41], $BiFeO_3$ [42], Fe_2O_3 [38], and $Sr_{0.95}Ca_{0.05}Ni_2V_2O_8$ [11]. This implies that the spin structure is unlike typical Ising systems where $z\vartheta$ has the value 9–10 (experiment) and 7–8 (theory) [44,45].

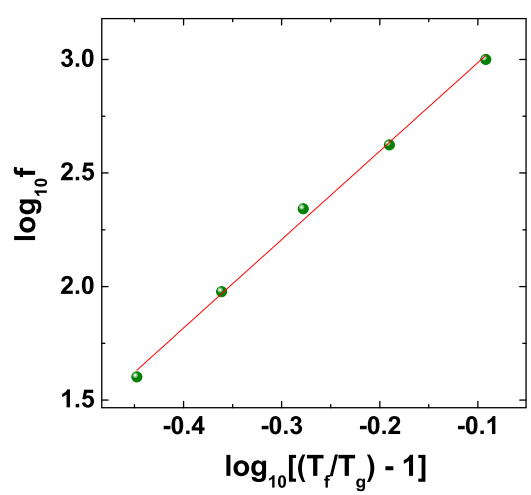

FIG. 7. (Color online) $\log_{10} f$ vs $\log_{10}[(T_f/T_g) - 1]$ for the Lu_2MnNiO_6 polycrystalline sample.

[1] L. Balents, Nature (London) **464**, 199 (2010).
[2] S. T. Bramwell and M. J. P. Gingras, Science **294**, 1495 (2001).
[3] N. Kawashima and H. Rieger, arXiv:condmat/0312432.
[4] K. Manna, D. Samal, S. Elizabeth, H. L. Bhat, and P. S. A. Kumar, J. Phys. Chem. C **115**, 13985 (2011).
[5] K. Manna, D. Samal, S. Elizabeth, H. L. Bhat, and P. S. A. Kumar, J. Supercond. Novel Magn. **24**, 833 (2011).
[6] K. Manna, D. Samal, A. K. Bera, S. Elizabeth, S. M. Yusuf, and P. S. A. Kumar, J. Phys.: Condens. Matter **26**, 016002 (2014).
[7] A. Jain, S. Singh, and S. M. Yusuf, Phys. Rev. B **74**, 174419 (2006).
[8] S. M. Yusuf, A. K. Bera, C. Ritter, Y. Tsujimoto, Y. Ajiro, H. Kageyama, and J. P. Attfield, Phys. Rev. B **84**, 064407 (2011).
[9] C. Ritter, S. M. Yusuf, A. K. Bera, Y. Goto, C. Tassel, H. Kageyama, A. M. Arevalo-Lopez, and J. P. Attfield, Phys. Rev. B **88**, 104401 (2013).
[10] K. Manna, D. Samal, S. Elizabeth, and P. S. A. Kumar, AIP Conf. Proc. **1512**, 1142 (2013).
[11] A. K. Bera and S. M. Yusuf, Phys. Rev. B **86**, 024408 (2012).
[12] K. Manna, S. Elizabeth, and P. S. A. Kumar, J. Appl. Phys. **113**, 17E114 (2013).
[13] D. Samal and P. S. A. Kumar, J. Appl. Phys. **111**, 043902 (2012).
[14] S. M. Yusuf, L. M. Rao, P. L. Paulose, and V. Nagarajan, J. Magn. Magn. Mater. **166**, 349 (1997).
[15] A. Das, S. K. Paranjpe, S. Honda, S. Murayama, and Y. Tsuchiya, J. Phys.: Condens. Matter **11**, 5209 (1999).
[16] J. O. Indekeu, Ph. de Smedt, and R. Dekeyser, Phys. Rev. B **30**, 495 (1984).
[17] A. C. D. van Enter and J. L. van Hemmen, Phys. Rev. B **31**, 603 (1985).
[18] M. M. Abd-Elmeguid, H. Micklitz, R.A. Brand, and W. Keune, Phys. Rev. B **33**, 7833 (1986).
[19] M. Gabay and G. Toulouse, Phys. Rev. Lett. **47**, 201 (1981).
[20] C. Sow, D. Samal, P. S. Anil Kumar, A. K. Bera, and S. M. Yusuf, Phys. Rev. B **85**, 224426 (2012).
[21] K. Manna, R. S. Joshi, S. Elizabeth, and P. S. Anil Kumar, Appl. Phys. Lett. **104**, 202905 (2014).
[22] K. Manna, V. S. Bhadram, S. Elizabeth, C. Narayana, and P. S. Anil Kumar, J. Appl. Phys. **116**, 043903 (2014).
[23] S. Maekawa, T. Tohyama, S. E. Barnes, S. Ishihara, W. Koshibae, and G. Khaliullin, *Physics of Transition Metal Oxides*, Springer Series in Solid-State Sciences (Springer, Berlin, 2004).
[24] J. Rodriguez-Carvajal, Physica B **192**, 55 (1993).
[25] T. Roisnel and J. Rodríguez-Carvajal, Mater. Sci. Forum **378-381**, 118 (2001).
[26] H. Eugene Stanley, *Introduction to Phase Transitions and Critical Phenomena*, (Oxford University Press, New York, 1971).
[27] A. Arrott and J. E. Noakes, Phys. Rev. Lett. **19**, 786 (1967).
[28] J. S. Kouvel and M. E. Fisher, Phys. Rev. **136**, A1626 (1964).
[29] H. Kawamura, J. Phys. Soc. Jpn. **61**, 1299 (1992); J. Phys.: Condens. Matter **10**, 4707 (1998).
[30] G. C. DeFotis and S. A. Pugh, Phys. Rev. B **24**, 6497 (1981).
[31] G. C. DeFotis and J. R. Laughlin, J. Chem. Phys. **84**, 3346 (1986).
[32] G. C. DeFotis, M. L. Laccheo, and H. A. Katori, Phys. Rev. B **65**, 094403 (2002).
[33] B. Yan, A. K. Paul, S. Kanungo, M. Reehuis, A. Hoser, D. M. Tobbens, W. Schnelle, R. C. Williams, T. Lancaster, F. Xiao, J. S. Moller, S. J. Blundell, W. Hayes, C. Felser, and M. Jansen, Phys. Rev. Lett. **112**, 147202 (2014).
[34] P. Giannozzi, S. Baroni, N. Bonini, M. Calandra, R. Car, C. Cavazzoni, D. Ceresoli, G. L. Chiarotti, M. Cococcioni, I. Dabo, A. Dal Corso, S. Fabris, G. Fratesi, S. de Gironcoli, R. Gebauer, U. Gerstmann, C. Gougoussis, A. Kokalj, M. Lazzeri, L. Martin-Samos, N. Marzari, F. Mauri, R. Mazzarello, S. Paolini, A. Pasquarello, L. Paulatto, C. Sbraccia, S. Scandolo, G. Sclauzero, A. P. Seitsonen, A. Smogunov, P. Umari, and R. M. Wentzcovitch, J. Phys. Condens. Matter **21**, 395502 (2009).
[35] J. P. Perdew, K. Burke, and M. Ernzerhof, Phys. Rev. Lett. **77**, 3865 (1996).
[36] H. Das, U. V. Waghmare, T. Saha-Dasgupta, and D. D. Sarma, Phys. Rev. Lett. **100**, 186402 (2008); Phys. Rev. B **79**, 144403 (2009).
[37] J. A. Mydosh, *Spin Glasses: An Experimental Introduction* (Taylor & Francis, London, 1993).
[38] M. D. Mukadam, S. M. Yusuf, P. Sharma, S. K. Kulshreshtha, and G. K. Dey, Phys. Rev. B **72**, 174408 (2005).
[39] M. D. Mukadam, A. Kumar, S. M. Yusuf, J. V. Yakhmi, R. Tewari, and G. K. Dey, J. Appl. Phys. **103**, 123902 (2008).
[40] K. Gunnarsson, P. Svedlindh, P. Nordblad, and L. Lundgren, Phys. Rev. Lett. **61**, 754 (1988).
[41] K. De, M. Thakur, A. Manna, and S. Giri, J. Appl. Phys. **99**, 013908 (2006).
[42] M. K. Singh, W. Prellier, M. P. Singh, R. S. Katiyar, and J. F. Scott, Phys. Rev. B **77**, 144403 (2008).
[43] N. Hanasaki, K. Watanabe, T. Ohtsuka, I. Kezsmarki, S. Iguchi, S. Miyasaka, and Y. Tokura, Phys. Rev. Lett. **99**, 086401 (2007).
[44] A. T. Ogielski, Phys. Rev. B **32**, 7384 (1985).
[45] S. Kirkpatrick and D. Sherrington, Phys. Rev. B **17**, 4384 (1970).